JOURNAL OF THE AMERICAN CHEMICAL SOCIETY

pubs.acs.org/JACS Article

Achieving High-Performance Defect-Free $LiCoO_2$ Cathode via a Dopant-Free Approach

Sichen Jiao,[#] Yu Li,[#] Ting Lin,[#] Shuhang Feng, Chengzhen Zhang, Hongyi Pan, Weiguang Lin, Xiqian Yu,* Lin Gu,* Xuejie Huang, Liquan Chen, and Hong Li*

Cite This: J. Am. Chem. Soc. 2025, 147, 22839−22850 Read Online

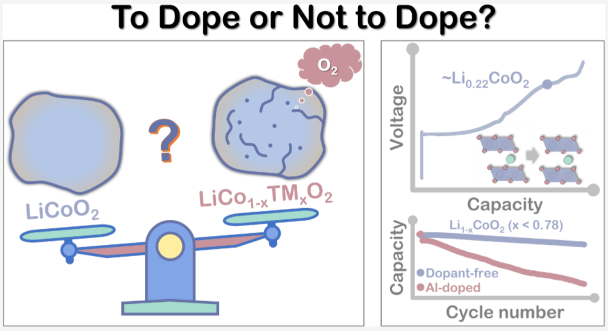

ABSTRACT: Elevating the charging voltage of layered oxide cathodes to achieve higher capacity induces phase transitions associated with transition metal slab gliding, which significantly impacts the material's structural stability. Doping with inert elements is commonly employed to delay such phase transitions to higher voltages. However, these electrochemically inactive elements do not participate in redox reactions, thereby compromising lithium storage capacity. This compromise raises a critical and underexplored issue regarding whether doped materials with reduced capacity still maintain an advantage in energy density. In this study, using $LiCoO_2$ as a model material, it was observed that an increase in the concentration of Al dopant indeed delayed the onset voltage of the H1−3 phase transition. However, the extent of delithiation associated with this phase transition remains largely unchanged. When the discharge capacity is controlled to just below the threshold for the global H1−3 phase transition, the undoped material demonstrates even superior capacity retention and rate performance compared to the doped samples, at a lower charging cutoff voltage. Comprehensive experimental characterizations and theoretical calculations reveal that the doping-induced structural defects hinder Li^+ conduction and promote oxygen release, consequently accelerating performance degradation. This study suggests that in the development of high-voltage layered oxide cathodes, it is crucial to prioritize enhancing material capacity. Additionally, it is imperative to meticulously assess the adverse effects of doping, as industrial preparation methods often lead to nonideal dopant incorporation, causing undesirable structural defects that are particularly harmful to the reversibility of high-voltage phase transitions.

1. INTRODUCTION

O3-type layered oxides are the most critical cathode materials for high-energy-density lithium-ion batteries, attributed to their densely packed oxygen-ion framework and well-defined two-dimensional lithium-ion conduction channels.[1,2] Since the discovery of the O3-type layered oxide cathode material, exemplified by $LiCoO_2$, by Professor J. Goodenough in 1980, and its subsequent commercialization by Sony in 1990, these materials have undergone extensive research and development over several decades.[3−5] Through compositional and structural adjustments, as well as optimizations in synthesis processes, the charging voltage of the layered oxide cathodes has been steadily elevated to achieve higher usable capacities, which are now approaching the bottleneck.[6−8] One of the primary limitations hindering further capacity enhancement is the necessity for these materials to undergo structural phase transitions involving transition metal slab gliding during high levels of delithiation.[9,10] These transitions induce significant lattice mismatches at phase boundaries, severely impacting the reversibility of the phase transformation.[11,12] Additionally, the instability of lattice oxygen under conditions of high delithiation and high charging voltage, coupled with the inherent chemical and electrochemical instability nature of carbonate liquid electrolytes, collectively contribute to the rapid degradation of material performance.[13,14]

Bulk phase doping remains the predominant approach to address the aforementioned issues. Over the past few decades, significant advancements have been achieved through the incorporation of a wide range of main-group, transition-metal, and rare-earth elements as dopants. Notably, inactive species such as Mg, Al, Ti, Nb, Mo and La have garnered particular attention in both lithium cobalt oxide ($LiCoO_2$, LCO) and nickel−manganese-cobalt ternary oxide systems ($LiNi_xMn_yCo_zO_2$, where $x + y + z = 1$, NMC).[15−19] Despite the specific mechanisms varying to some extent among different dopants, their overarching objectives include mitigating phase transitions and lattice distortions, as well as

Received: March 26, 2025
Revised: May 21, 2025
Accepted: June 11, 2025
Published: June 17, 2025

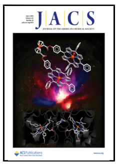

https://doi.org/10.1021/jacs.5c05162
J. Am. Chem. Soc. 2025, 147, 22839−22850

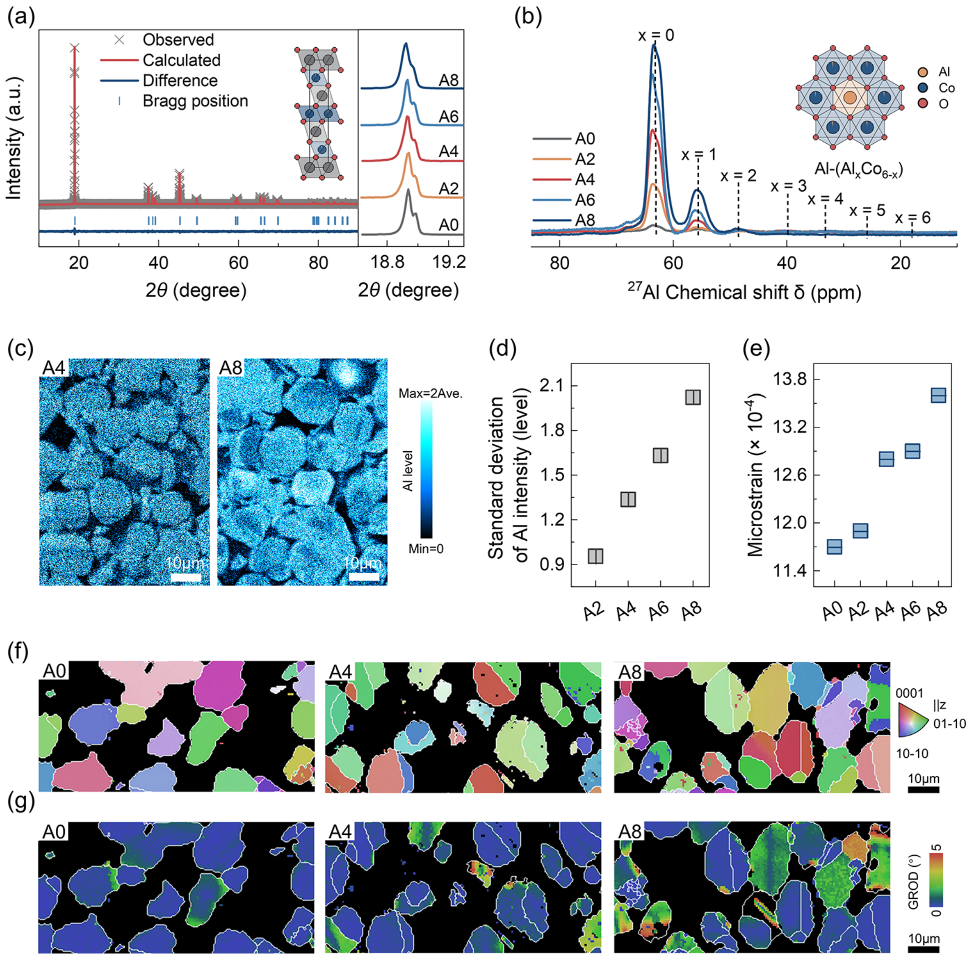

Figure 1. Structural characterizations of LCO materials. (a) XRD patterns of LCO materials, with the unit cell shown in the inset, where gray, blue, and red spheres represent Li, Co, and O atoms, respectively. The (003) diffraction peaks for A0−A8 are highlighted on the right. Herein, a series of Al-doped LCO samples ($LiCo_{1-x}Al_xO_2$) with varying Al doping concentrations are denoted as follows: A0 (0 ppm Al, $x = 0$), A2 (2000 ppm Al, $x = 0.007$), A4 (4000 ppm Al, $x = 0.015$), A6 (6000 ppm Al, $x = 0.022$), and A8 (8000 ppm Al, $x = 0.030$). (b) Selected regions of the ^{27}Al ssNMR spectra for A0−A8, where dashed lines indicate distinct Al environments. Schematic depictions illustrate Al environments with varying numbers of Co atoms in the second coordination shell. (c) Cross-sectional EPMA elemental maps of Al for samples A4 and A8, with the color bar maximum set to twice the average intensity of the sample. (d) The standard deviation of the Al intensity distribution, derived from statistical analysis of EPMA images for A2−A8. (e) Microstrain evolution in A0−A8, determined via Williamson−Hall analysis based on refined synchrotron X-ray diffraction patterns. (f) EBSD inverse pole figure maps illustrating the grain and subgrain orientations in the cross sections of A0 (left), A4 (middle), and A8 (right). (g) Grain reference orientation deviation maps derived from the EBSD orientation data for A0, A4, and A8, reflecting lattice misorientation within individual grains.

stabilizing reactive oxygen species, thereby collectively enhancing cycling stability.[20,21] However, as the material's charging voltage is progressively increased to achieve higher and more stable capacities, it often becomes necessary to elevate the concentration or variety of doping elements.[22−24] Although this method can indeed enable higher charging voltages, the resultant capacity enhancement is often marginal due to the generally nonelectrochemically active nature of the dopants.[22,25] Additionally, elevating the charging voltage poses significant challenges to the design of battery material systems, particularly for electrolytes.

On the other hand, as the dopant concentration increases, a significant challenge arises regarding whether industrially scalable synthesis methods can achieve uniform incorporation of dopant elements into the cathode oxide lattice.[16,26] For instance, Duffiet et al. observed chemical inhomogeneity in Al-doped LCO cathodes, with Al-rich domains forming even at a moderate Al doping level (4 at%), despite the absence of long-range phase separation.[27] This inhomogeneous distribution of chemical elements can result in various types of structural defects within the material, such as dislocations, stacking faults, twin boundaries, antiphase boundaries, and domain boundaries, deviating from the ideal single-crystal layered structure.[28−30] In recent years, researchers have increasingly recognized that these structural defects are closely associated with performance degradation, including irreversible capacity loss and oxygen instability, which are key factors limiting the reversibility of materials in high-voltage operation.[28,31,32] Therefore, it is imperative to revisit the conventional wisdom of doping, specifically whether we can rely on bulk phase doping to inhibit or mitigate the detrimental phase transition of layered oxide cathode materials, considering not just the charging voltage but also the achievable capacity, to achieve higher energy density over extended cycling.[25,33]

In this work, we investigate LCO cathodes as a model system, systematically incorporating industrially relevant levels of Al doping. Contrary to expectations, decent level Al doping fails to delay the onset capacity of the high-voltage H1−3

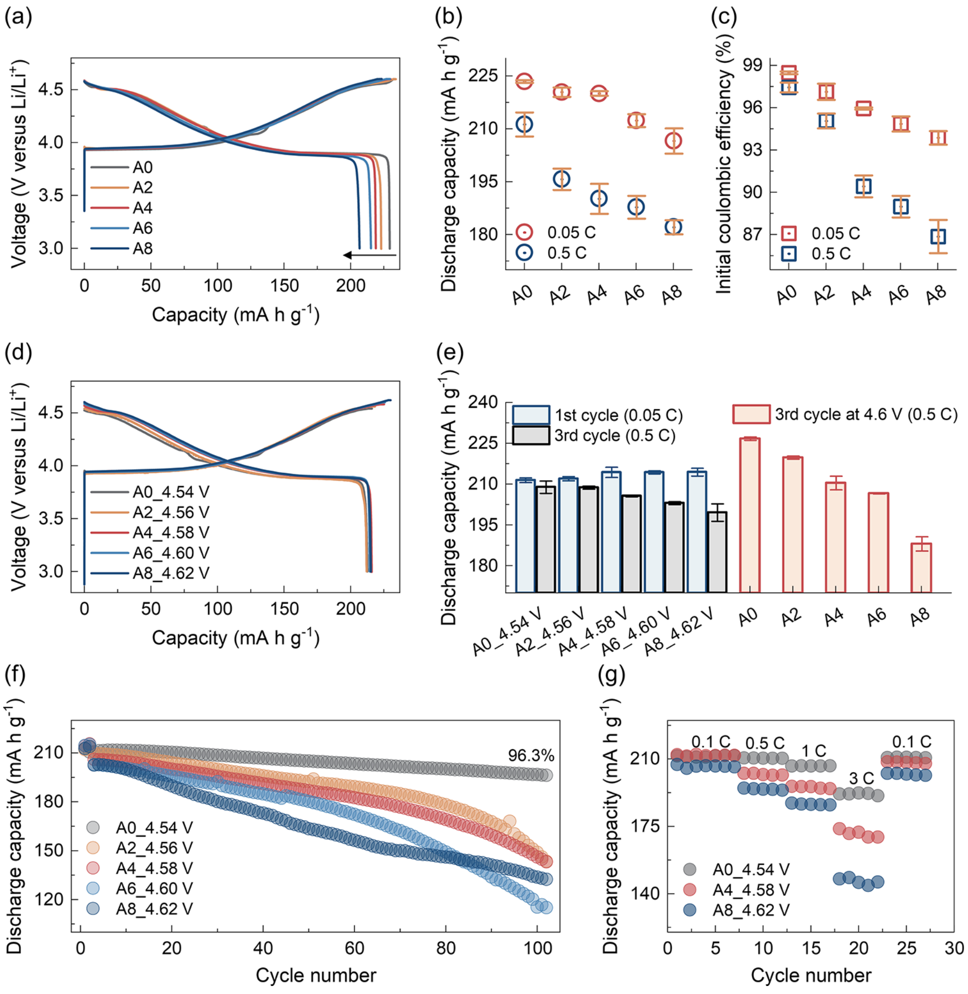

Figure 2. Electrochemical evaluation of LCO materials. (a) First-cycle voltage profiles of A0−A8 measured at 0.05 C and 25 °C with a fixed cutoff voltage of 4.6 V (vs Li/Li$^+$), where 1 C = 274 mA/g. (b) Summary of first-cycle discharge capacities and (c) initial Coulombic efficiencies for A0−A8 at 0.05 and 0.5 C under a cutoff voltage of 4.6 V. (d) First-cycle voltage profiles of A0−A8 at 0.05 C under varying cutoff voltages, tailored to the Al dopant content to achieve comparable discharge capacities across the materials: A0 at 4.54 V, A2 at 4.56 V, A4 at 4.58 V, A6 at 4.60 V, and A8 at 4.62 V. (e) Summary of discharge capacities at varying cutoff voltages at 0.05 C (first cycle) and 0.5 C (third cycle) and comparison of third-cycle discharge capacities at 4.6 V at 0.5 C (third cycle). (f) Cycling performance of A0−A8 at 0.5 C and 25 °C operating at a comparable discharge capacity across samples (with the initial two activation cycles at 0.05 C). (g) Rate performance testing of A0, A4, and A8, with two initial cycles at 0.05 C, where the cutoff voltage was adjusted to ensure a comparable initial capacity.

phase transition, despite an elevation in the onset voltage. Meanwhile, comprehensive multilength scale experimental characterizations and theoretical calculations reveal two key adverse effects of Al doping: chemical and structural heterogeneities at the particle level, which can lead to structural degradation and impede lithium diffusion. Doping-induced capacity loss necessitates charging the Al-doped LCO to a higher voltage to attain a capacity comparable to that of the undoped counterparts. Electrochemical evaluations reveal that Al doping offers no discernible advantages when the initial discharge capacity is fixed at ∼ 210 mAh/g (right below the onset capacity of the H1−3 phase transition). In contrast, the dopant-free LCO demonstrates exceptional electrochemical performance during extended cycling (∼210 mAh/g at 4.54 V vs Li/Li$^+$), in terms of energy density, capacity retention, and rate capability. Our work revisited the long-held perception that doping strategies are overwhelmingly beneficial, highlighting the overlooked negative effects of doping and providing fresh insight for designing high-capacity and long-standing oxide cathode materials

2. RESULTS

2.1. Characterizations of Al Doping in LCO Structure.

The synthesis of a series of Al-doped LCO cathode materials was validated through inductively coupled plasma optical emission spectrometer (ICP-OES) results, as detailed in Table S1. The materials, denoted as $LiCo_{1-x}Al_xO_2$, exhibit Al contents ranging from 0 to 8000 ppm, corresponding to ∼ 0.7, ∼ 1.5, ∼ 2.2, and ∼ 3.0 at% Al for A2 (2000 ppm), A4 (4000 ppm), A6 (6000 ppm), and A8 (8000 ppm), respectively. The undoped material is referred to as A0. All samples crystallize into single primary particles with average sizes of 12−15 μm (Figure S1), and the larger particle size is crucial for the practical application of LCO cathodes. X-ray diffraction (XRD) patterns confirm the $R\bar{3}m$ space group of pure-phase LCO (Figures 1a and S2). As the Al content rises, the (003) diffraction peak (∼19°) shifts progressively toward lower angles, reflecting an expansion of the lattice parameter along the *c*-axis. Solid-state nuclear magnetic resonance (ssNMR) was used to investigate the local chemical environment of Al dopants. As shown in Figure 1b, the ^{27}Al ssNMR spectra of all doped samples exhibit similar profiles, with signal intensity scaling with Al content (Figure S3). These signals correspond to Al in second-coordination-shell environments with varying numbers of low-spin Co^{3+} ions (e.g., Al-(Al_xCo_{6-x})).[27] For instance, the peak at ∼ 63 ppm is attributed to Al atoms surrounded exclusively by Co^{3+} ions ($x = 0$). Importantly, no signals near ∼ 18 ppm ($Al(Al_6)$, $x = 6$) were detected, confirming that the Al element was successfully incorporated into Co sites without segregation of Al-rich domains (e.g., $LiAlO_2$-like) at the local scale. The stoichiometry of A0 to A8 was further verified through ^7Li ssNMR spectra (Figure S4). Moreover, X-ray pair distribution function (XPDF) analysis shows that the local coordination environments of Co atoms remain virtually unchanged after Al doping (Figure S5 and Table S2).

To extend the analysis beyond the atomic scale, electron probe microanalysis (EPMA) was employed to investigate the particle-level distribution of Al dopants, leveraging its high sensitivity to trace elements. The EPMA image of the A8 sample reveals a distinctly nonuniform Al distribution, characterized by localized regions of varying concentrations (Figure 1c). Moreover, the standard deviation of Al intensity signals increases progressively from A2 to A8 (Figures 1d and S6), signifying the rising chemical heterogeneity with higher doping levels. Structural inhomogeneity, often associated with chemical variations, was further examined using synchrotron X-ray diffraction (SXRD) measurements followed by Le Bail refinement (Figure S7 and Table S3). Williamson-Hall strain analysis of the refined profiles reveals an accumulation of microstrain as the Al doping concentration increases (Figures 1e and S8), mirroring the trends observed in chemical heterogeneity. In addition, cross-sectional electron backscatter diffraction (EBSD) measurements were performed to gain crystallographic information at the particle scale. The inverse pole figure (IPF) maps (Figure 1f) show regions of different colors within single particles, delineated by white lines, indicating subgrain boundaries. The presence of these imperfect boundary regions suggests the existence of defects in "single-crystalline" LCO particles. Notably, these subgrain boundaries become more prevalent in the A4 and A8 samples. The intragranular lattice orientation variation is visualized in the grain reference orientation deviation (GROD) maps (Figure 1g), where higher GROD values reflect increased lattice distortion and strain accumulation. As Al doping intensifies, the microsized LCO particles are heterogeneously strained and exhibit an increased density of lattice defects (Figure S9). These particle-scale observations align with SXRD findings, demonstrating that Al doping exacerbates the structural heterogeneity of LCO. In contrast, the undoped A0 sample displays nearly ideal crystallinity throughout the whole particle. Based on the aforementioned results, Al was successfully incorporated into the crystal structure of LCO. However, as the Al doping concentration increased, the distribution of Al elements within the structure became increasingly heterogeneous, resulting in a greater prevalence of high-dimensional defects. This, in turn, led to an increase in the internal strain of LCO particles.

2.2. Impact of Al Doping on the Electrochemical Performance of LCO.

To investigate the impact of Al doping on the electrochemical performance of LCO, half-cell tests were performed at 25 °C. Under a consistent cutoff voltage of 4.6 V (Figure 2a), the first cycle discharge capacity decreases markedly, from 229.5 mAh/g for A0 to 206.8 mAh/g for A8 at 0.05 C (1 C = 274 mA/g). Galvanostatic testing reveals a gradual reduction in discharge capacity (Figure 2b) and initial Coulombic efficiency (Figure 2c) as Al content increases, a trend that becomes more pronounced at higher current densities (Figure S10). This indicates that the capacity loss is largely governed by lithium diffusion kinetics (Figure S11). Regarding the cycling performance at 4.6 V, A8, with the highest Al doping, maintains 92.0% of its initial capacity after 80 cycles at 0.5 C, surpassing other samples (Figure S12). This seems to be consistent with the reported positive effects of Al doping in the literature.[16,18,22] However, this improvement comes at the cost of an initial capacity loss of approximately 42.3 mAh/g at 0.5 C, compared to A0. The reduced capacity upon cycling suggests that fewer lithium ions are inserted and extracted from A8, likely stabilizing the structure by maintaining a less delithiated state. Furthermore, the diminished discharge capacity lowers the overall energy density, raising concerns about the practical benefits of the seemingly favorable cycling performance of A8 at 4.6 V.

What matters most is the material's actual energy density, making it essential to evaluate the cycling performance of A0–A8 with comparable initial discharge capacity or energy density. To this end, a comparable initial discharge capacity of ∼ 210 mAh/g was achieved at 0.05 C by adjusting the cutoff voltages in accordance with Al content: A0 at 4.54 V, A2 at 4.56 V, A4 at 4.58 V, A6 at 4.60 V, and A8 at 4.62 V (Figure 2d). LCO with higher Al content requires a higher charging voltage to match the discharge capacity of the lower-Al variants. Moreover, the difference in usable capacity during cycling (third cycle after activation process) at 0.5 C was reduced to ∼ 9 mAh/g (gray columns in Figure 2e), compared to ∼ 38 mAh/g at a constant voltage of 4.6 V (orange columns). Surprisingly, the A0 sample, free from doping, exhibits unprecedented cycling performance with an initial capacity of 210.8 mAh/g at 0.5 C and 96.3% retention over 100 cycles at 4.54 V (Figure 2f). This dopant-free LCO also outperforms all other samples in terms of material-level energy density (Figure S13). With a usable capacity of ∼ 210 mAh/g, the voltage profile of A0 remains stable during cycling, highlighting its structural integrity (Figure S14). Furthermore, A0 achieves superior rate performance compared to the doped LCO materials, delivering an impressive capacity of ∼ 192 mAh/g at 3 C (Figure 2g). It is important to note that once the cutoff voltage of the A0 material exceeds 4.54 V, such as during cycling at 4.6 V, it experiences rapid degradation. This suggests the existence of a critical voltage or capacity threshold for achieving optimal cycling stability, as we will discuss later. Overall, our results show that with a higher lithium usage ratio ($Li_{1-x}CoO_2$, $x = \sim 0.78$ Li, corresponding to ∼ 210 mAh/g), Al doping fails to stabilize the layered structure and instead leads to rapid performance degradation. In contrast, dopant-free LCO demonstrates remarkable cycling stability with high capacity at 4.54 V, particularly concerning energy density.

2.3. Analysis of Al Doping Effect on High-Voltage Phase Transition.

In the case of A0–A8 in this study, surface-related factors are unlikely to account for the rapid degradation observed in the Al-doped materials, as all LCO samples are coated with a nanoscale solid electrolyte that we developed before, showing effectively minimized side reactions (Figure S15).[34] Therefore, it is crucial to examine the influence of Al doping on bulk phase transitions in LCO. Upon charging, pure LCO (A0) undergoes distinct phase transitions, visible as voltage plateaus (Figure S16). In the high-voltage region, the

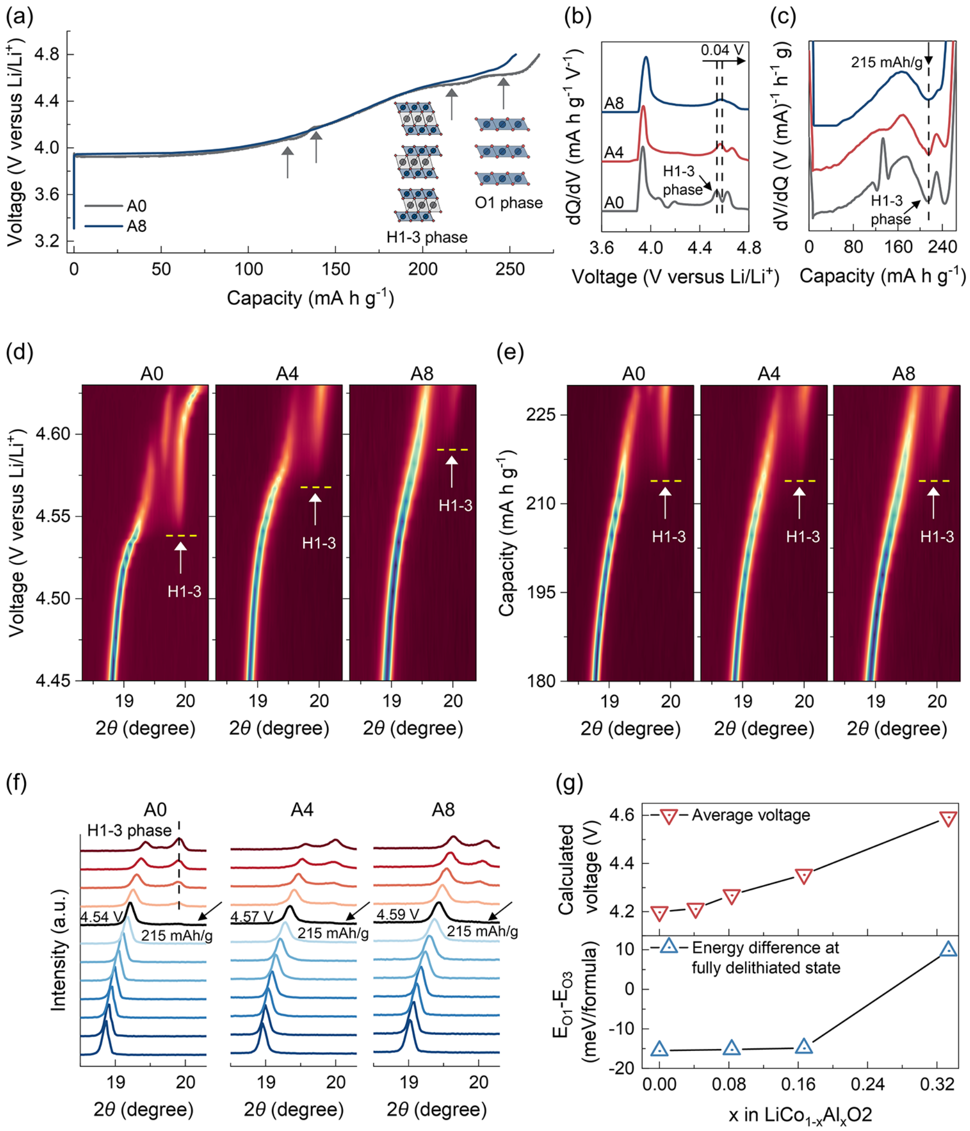

Figure 3. Effect of Al doping on phase transitions in LCO materials. (a) First-cycle charging curves of A0 and A8 up to 4.8 V (vs Li/Li$^+$) at 0.05 C. In A0, a series of voltage plateaus are indicated by a gray arrow, with the structure of the H1−3 and O1 phases schematically shown below. (b) dQ/dV and (c) dV/dQ analyses of the charging curves up to 4.8 V for A0, A4, and A8, where the peak corresponding to the H1−3 phase transition is marked by a black arrow. Selected in situ XRD contour plots of A0, A4, and A8 illustrating the evolution of the (003) peak during charging as a function of (d) voltage and (e) capacity. (f) Enlarged XRD patterns of A0, A4, and A8, highlighting the (003) peak position of the H1−3 phase (dashed line) and the onset of the H1−3 transition (black arrow). (g) DFT-calculated average voltages of LCO (upper panel) and energy differences between the fully delithiated O1 and O3 phases (lower panel) as a function of Al content.

delithiated O3-type phase first transforms into a hybridized O3/O1 phase (H1−3) at ∼ 4.54 V, followed by the coexistence of H1−3 and O1 phases at ∼ 4.62 V (Figure 3a).[9] In contrast, Al-doped LCO (A8) exhibits a more solid-solution-like behavior, with smoothed voltage profiles around ∼ 4.2 and 4.6 V. Differential capacity (dQ/dV) analysis highlights these differences (Figure 3b). The peaks near 4.2 V, clearly observed in A0, disappear upon trace Al doping, suggesting that Al effectively suppresses the corresponding phase transition. This voltage plateau is associated with a monoclinic transition, driven by lithium-vacancy ordering around $x \approx 0.5$ ($Li_{0.5}CoO_2$). Previous studies have demonstrated that this transition is highly sensitive to local structural perturbations within the Co layers, and can be hindered by even slight lithium excess or dopant incorporation.[27,35] Therefore, the sloped voltage profiles in Al-doped LCO can be attributed to Co/Al disorder introduced by Al substitution. At higher voltages, the sharp H1−3 and O1 peaks in A0 broaden in A4 and merge into a single broad peak in A8, with H1−3 peak positions shifting incrementally from 4.54 V (A0) to 4.56 V (A4) and 4.58 V (A8). The gradual increase in voltage can be attributed to the enhanced bonding strength of Al−O bonds, in line with well-established doping principles.[36] Indeed, several dopants of nonactive elements, such as Al, Nb, Mn, and Ti, have been shown to effectively delay the onset voltage of high-voltage phase transitions in LCO materials.[16−18,37] However, when considering capacity instead of voltage, it is surprising to note that Al doping has almost no effect on the capacity associated with the H1−3 transition in the differential voltage (dV/dQ) curves, as evidenced by a consistent peak position around ∼ 215 mAh/g across all samples (Figure 3c). The decoupling of onset voltage and

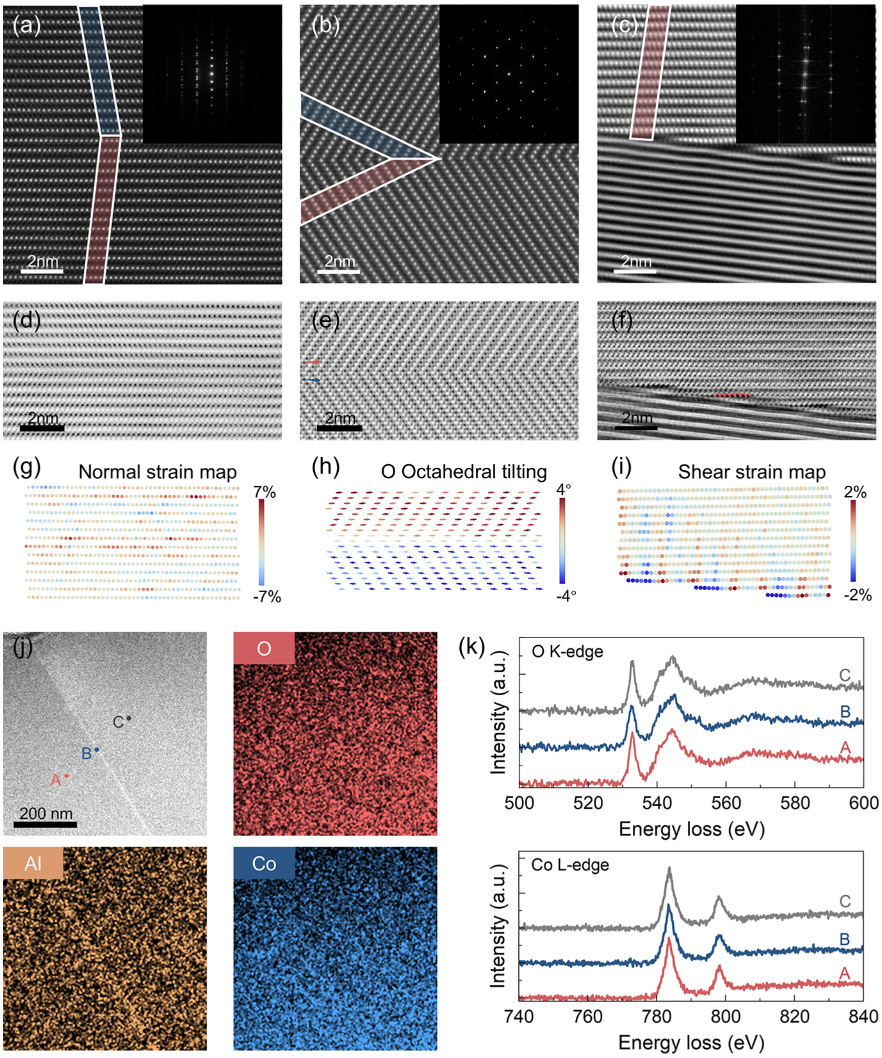

Figure 4. Atomic-scale characterizations of 2D defects in Al-doped LCO STEM-HAADF images of (a) stacking fault; (b) twin boundary; and (c) incoherent boundary within the A8 sample, where corresponding FFT images are shown in insets. STEM-ABF images of the different types of boundaries showing the arrangement of oxygen atoms in (d) stacking fault; (e) twin boundary; (f) incoherent boundary, where the variation in O environment is indicated by an arrow, and the potential Al concentrated sites are circled. (g) Normal strain map demonstrates the uniform interlayer distance at the stacking fault. (h) O coordination map evaluates the off-centering degree of O away from neighboring atoms at the twin boundary due to symmetry constraints. (i) Shear strain map shows the intralayer bending of the Co slab at the inherent boundary. (j) STEM-EDS mapping shows a uniform distribution of O and Co elements but a concentrated Al near the defective boundary region. (k) Normalized STEM-EELS reveals a drop in the O pre-edge peak at the boundary and an unchanged Co L-edge peak.

capacity is further corroborated by quasi-equilibrium voltage profiles obtained through galvanostatic intermittent titration technique (GITT) (Figure S17). This result proves that Al doping elevates the onset voltage of the H1−3 transition while leaving the maximum lithium extraction prior to its initiation unchanged (~$Li_{0.78}$ for both A0 and A8). This amount of lithium extraction precisely corresponds to the critical capacity for stable cycling in A0, as mentioned above. Specifically, A0 maintains excellent stability with a capacity of ~ 210 mAh/g, without triggering the H1−3 phase transition (just below the onset capacity of ~ 215 mAh/g). However, once this capacity is surpassed and the H1−3 phase transition is involved, A0 cycled at 4.6 V exhibits rapid capacity decay.

In-situ XRD measurements were conducted to monitor phase transitions through structural responses (Figure S18). The H1−3 phase, characterized by slab distance collapse, is evidenced by the evolution of the (003) peak, shown as a function of voltage and capacity in Figure 3d,e, respectively. A newly observed diffraction peak at higher angles, indicative of the H1−3 phase, shifts to higher voltages in LCO with increasing Al content but remains nearly constant with respect to capacity. Detailed analysis shows that the onset voltage for the H1−3 transition increases from 4.54 V in A0 to 4.59 V in A8 (a 0.05 V shift), while the onset capacity remains ~ 215 mAh/g (Figure 3f). These findings, consistent with dQ/dV and dV/dQ analyses, confirm that Al doping does not enable greater lithium extraction without triggering the H1−3 transition, though it raises the onset voltage. The divergence between the onset voltage and capacity of the H1−3 transition can be rationalized thermodynamically. Density functional theory (DFT) calculations reveal that Al content linearly increases the average voltage of LCO, even at low doping levels (~4 at%) (upper panel of Figures 3g and S19). However, significant stabilization of the delithiated O3 phase against the O1 phase occurs only at higher Al concentrations (>16 at%), as shown in the lower panel of Figure 3g. Previous studies have

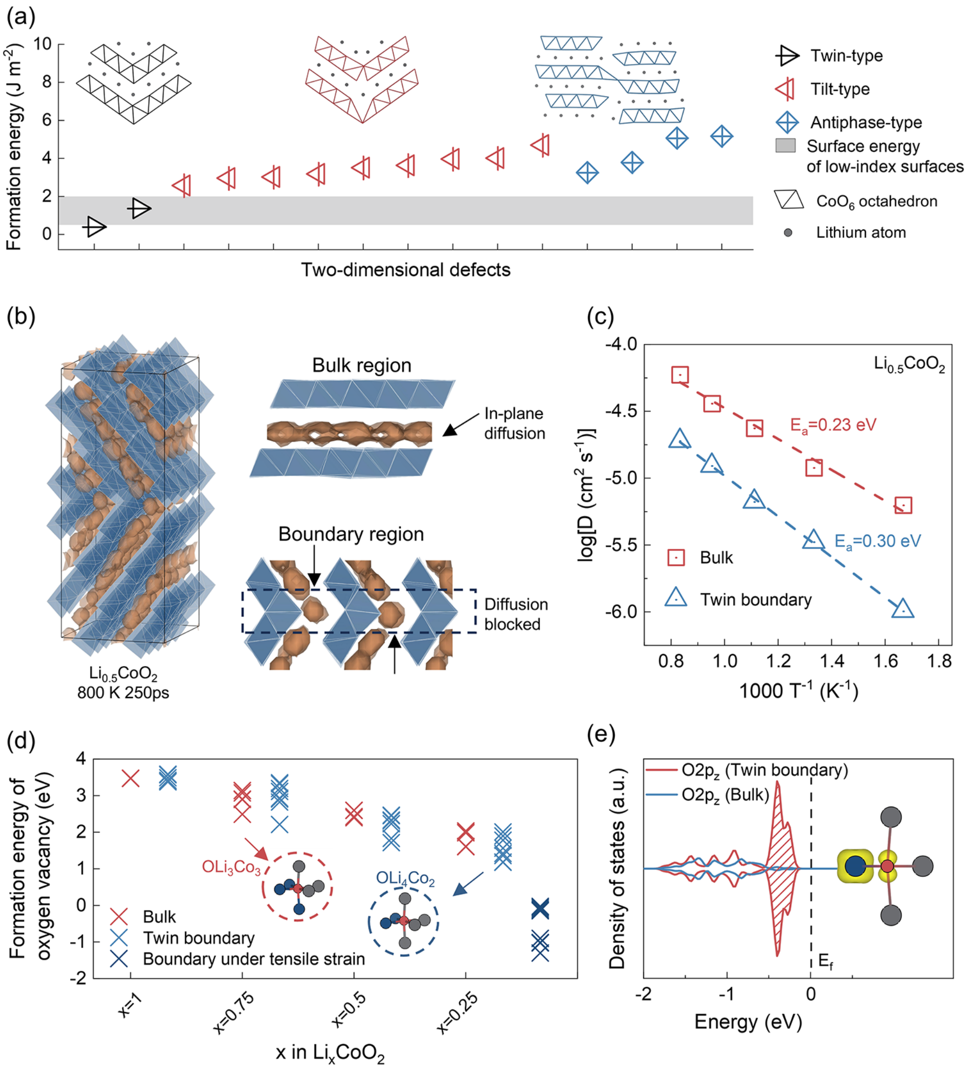

Figure 5. Theoretical investigation of 2D defects in LCO (a) Calculated formation energies of various 2D defects in LCO, including twin-type (black), tilt-type (red), and antiphase-type (blue) boundaries, with schematic representations of the defect structures shown in the inset. (b) Probability densities of lithium ions (brown isosurface) obtained from 250 ps DPMD simulations at 800 K for the $Li_{0.5}CoO_2$ structure containing twin boundary (only the CoO_6 octahedrons were shown in blue-gray for clarity). The comparison of Li probability densities in the perfect and boundary regions is displayed on the right, highlighting blocked lithium diffusion (dashed box). (c) Arrhenius plots of lithium diffusivity in perfect and boundary-containing $Li_{0.5}CoO_2$ at various temperatures, derived from DPMD simulations. (d) Calculated formation energies of oxygen vacancies in perfect bulk and boundary-containing LCO at different states of delithiation. Insets illustrate the distinct local coordination environments of oxygen atoms. Gray, blue, and red spheres represent Li, Co, and O, respectively. (e) Calculated pDOS for oxygen atoms located in the bulk region (OLi_3Co_3) and at the twin boundary (OLi_4Co_2). The isosurface of charge density around an OLi_4Co_2 atom within the energy range of −0.5 to 0 eV is shown (dashed region in pDOS).

primarily focused on the relationship between doping and the voltage at which phase transitions are triggered, often overlooking the corresponding capacity (lithium content). As a result, it is intuitively believed that doping can delay or inhibit high-voltage phase transitions in layered oxide cathodes. In contrast to this conventional view, we found that a decent level of Al doping has ignorable impacts on the onset capacity of the H1−3 phase transition in LCO, and thus fails to stabilize the bulk structure of high-capacity LCO materials. Therefore, the enhanced cycling performance of A8 at a constant 4.6 V is more likely attributed to the reduced extent of lithium extraction, which outweighs the structural stabilization effect provided by Al doping.

2.4. Understanding of the Structural Heterogeneity in Microsized LCO Particles. Despite cycling under a controlled capacity (~210 mAh/g), the rapid performance degradation of Al-doped LCO remains unclear, as all LCO materials operate below the onset capacity of the H1−3 phase transition. Given the increased chemical and structural heterogeneity with rising Al content, a detailed microstructural analysis of the microsized LCO particles is necessary to elucidate the underlying causes. Figure S20 displays a series of transmission electron microscopy (TEM) images of typical A8-LCO, highlighting the planar defects of interest with the orange arrows. This result accords with EBSD results that the doping of Al tends to introduce structural heterogeneity at the particle level. Different types of two-dimensional (2D) defects were further identified by scanning transmission electron microscopy high-angle annular dark field (STEM-HAADF) imaging, which probed the atomic arrangement at these defective boundaries. Figure 4a shows a stacking fault, where only a change in the stacking orientation of transition metal

https://doi.org/10.1021/jacs.5c05162
J. Am. Chem. Soc. 2025, 147, 22839−22850

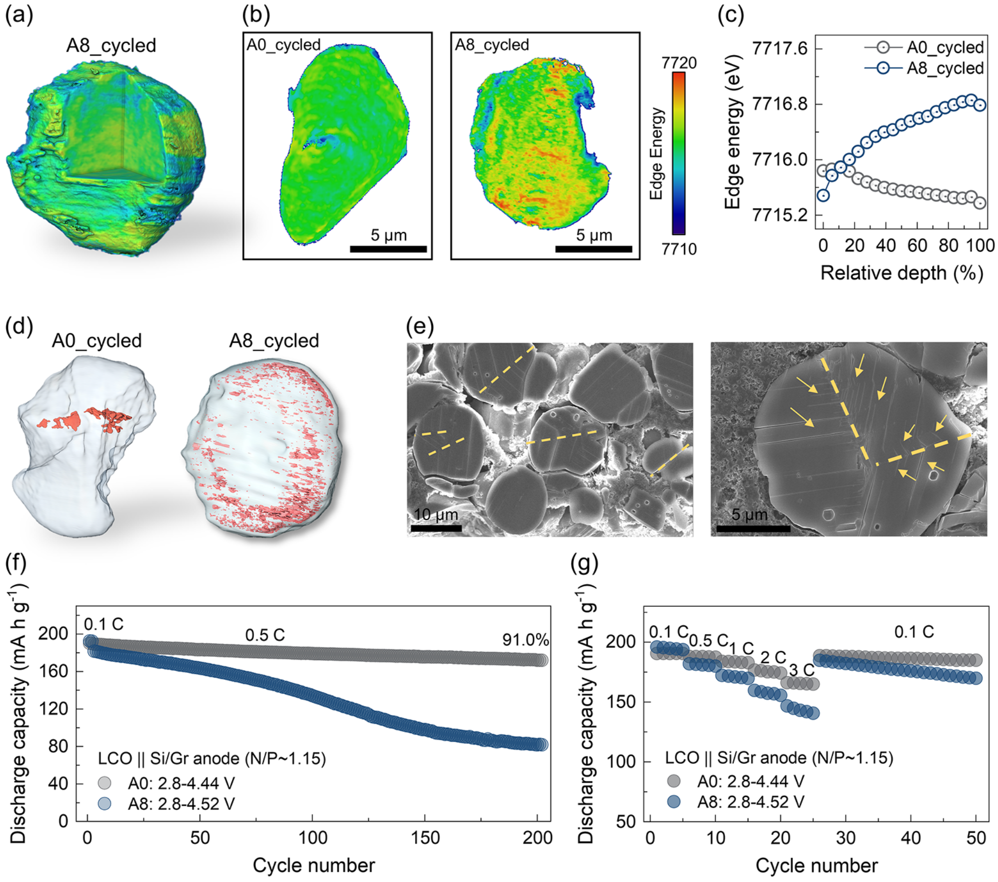

Figure 6. Reaction homogeneity and structural stability during cycling (a) 3D rendering of TXM-XANES data for A8 particle after 100 cycles in a half-cell at 4.62 V. (b) 2D slices extracted from the 3D TXM-XANES images of cycled A0 and A8 particles at 4.54 and 4.62 V, respectively, with a scale bar indicating 5 μm. (c) Depth profile analysis of Co K-edge energy distributions in cycled A0 and A8 particles, illustrating variations across the particle interiors. (d) 3D rendered images of cycled A0 and A8 particles, highlighting crack regions in red to emphasize structural degradation. (e) Cross-sectional SEM images of A8 electrodes after half-cell cycling. Yellow dashed lines mark twin-like cracks along the boundaries. (f) Full-cell cycling performance of A0 and A8 with Si/Gr anodes at 0.5 C, with the cutoff voltage of 4.44 and 4.52 V, respectively (including the initial two activation cycles at 0.1 C). (g) Rate performance of A0 and A8, where the cutoff voltage was set as 4.44 and 4.52 V for A0 and A8, respectively.

ions occurs. This characteristic could be explicitly distinguished by the FFT images with the axis of symmetry along the horizontal axis. Figure 4b displays a twin boundary leaving a "V" shape atomic arrangement. At this type of boundary, the two (0003) planes intersect at an angle of 109.5°, with the atomically defined twin boundary precisely aligned along the (−1104) plane. Additionally, an incoherent boundary was observed, where the top LCO layer, viewed along the [100] direction, intersects with a rotated layer beneath (Figure 4c). STEM annular bright field (ABF) was used to examine the light atoms within the defective regions. Regarding the oxygen atoms, while their arrangement remains unchanged at the stacking fault (Figure 4d), the oxygen atoms residing at the twin boundary are constrained to the Co plane due to the mirror symmetry (Figure 4e), in contrast to the nearby oxygen atoms located away from the Co plane. Notably, distinct atomic contrast can be found at the end of the bent Co layer in the ABF images (Figure 4f), suggesting a potential accumulation of Al element at the boundary region. Quantitative analysis of atomic position reveals the strain distribution at the boundary (Figure S21). In contrast to the stacking faults, which introduce no residual strain and resemble the perfect layered structure (Figures 4g and S22), a markedly distorted coordination environment of oxygen atoms is observed near the twin boundary. This is evidenced by the map showing the tilting of oxygen octahedra relative to neighboring cobalt ions (Figure 4h). Moreover, the incoherent boundary exhibits evident shear strain, as confirmed by the bending of the layered structure and the corresponding strain mapping (Figure 4i). STEM energy dispersive X-ray spectroscopy (EDS) was performed to analyze the elemental distribution and further explore the relationship between boundary formation and Al doping. As shown in Figures 4j and S23, Co and O elements are uniformly distributed, whereas the Al distribution reveals a distinct linear feature aligned with the crystallographic boundary. This finding suggests the potential role of Al doping in the formation of 2D defects in LCO, which coincides with recent studies that report Al-dopant-induced twinned structure within Ni-rich layered cathodes.[38] Further electron energy loss spectroscopy (EELS) analysis reveals the electronic structure of O and Co near the boundary region. A decline in the O pre-edge peak is observed at the boundary, indicating a weakened hybridization between the O 2p and Co 3d orbitals (Figures 4k and S24). This suggests a loss of oxygen stability in the boundary region. In contrast, the electronic structure of Co remains unchanged in terms of the position and area of its L-edge peak, thus implying an Al−O interaction at the boundary.

The distinct atomic arrangements observed within the boundary regions can significantly affect lithium diffusion and structural stability of LCO, insights that can be gained through theoretical calculations. However, traditional DFT and ab initio molecular dynamics methods face huge challenges in modeling 2D defects and their structural evolution, due to the inherent limitations in their spatial and temporal scales. To overcome these constraints, machine-learning-based large-scale atomic simulations were employed to explore the impact of 2D defects, which have proven effective in studying large systems while maintaining DFT-level accuracy, both in the field of batteries and beyond.[39−42] Specifically, a deep learning-based potential model (DP potential model), trained on an extensive data set of high-accuracy DFT calculations, was developed to encompass a wide range of compositions and structures in LCO systems (Figures S25−S27 and Note S1). Various 2D defect types were assessed by calculating their formation energies (Figure S28). As shown in Figure 5a, the twin-type boundary emerges as the most energetically favorable, consistent with our STEM results and its prevalence in layered oxide cathode materials reported before.[29,31,32] Boundaries with fewer dangling Co−O bonds exhibit formation energies comparable to the surface energies of low-index surfaces, highlighting the feasibility of 2D defect formation in LCO. Long-time scale deep potential molecular dynamics (DPMD) simulations were conducted to investigate lithium diffusion in perfect LCO and the defective one. Probability density maps of Li atoms derived from these simulations reveal continuous in-plane diffusion pathways in perfect LCO, whereas conduction channels across the twin boundaries are largely obstructed (Figure 5b). As indicated by the black arrow, the boundary region (dashed rectangular box) shows minimal lithium-ion occupancy and a discontinuous Li density distribution. Lithium diffusivity was further calculated across a range of temperatures and fitted to the Arrhenius equation (Figures S29 and S30). As illustrated in Figure 5c, lithium diffusion exhibits a higher activation energy (Ea) in structural models containing twin boundaries (0.30 eV) compared to defect-free bulk structures (0.23 eV). Impeded Li-diffusion can exacerbate strain accumulation at boundaries and compromise rate performance. Regarding structural stability, formation energy calculations for oxygen vacancies indicate that oxygen atoms within boundary regions are more likely to be released, particularly in highly charged states (Figures 5d and S31).[28] This instability arises from its distinct local coordinating environment, where oxygen atoms in Li-rich or under-coordinated environments are concentrated near the boundaries, compared to that in the perfect LCO (OLi_3CoO_3). Partial density of states (pDOS) calculations reveal that Li-rich oxygen environments (OLi_4Co_2) residing at the twin boundary contribute significantly to states just below the Fermi level (Figure 5e), suggesting these oxygen atoms are preferentially depleted of electrons during delithiation.

2.5. Reversible Cycling of Dopant-Free LCO and Full-Cell Performances. To elucidate the impact of Al doping on the structural and chemical stability of LCO during extended cycling, comparative analyses were conducted on A0 and A8 cycled at 4.54 and 4.62 V, respectively. Synchrotron-based transmission X-ray microscopy coupled with X-ray absorption near-edge structure spectroscopy (TXM-XANES) was employed to examine reaction homogeneity by mapping the elemental distribution and valence states within a single particle in three-dimensional (3D) space. 3D TXM-XANES images were collected near the Co K-edge for cycled particles (Figure 6a), where a broader edge energy distribution can be found in cycled A8 (Figure S32). 2D slice of the 3D TXM-XANES image shows widespread localized regions with high and low Co valence states throughout the A8 particle, highlighting its reaction heterogeneity (Figure 6b). Further depth profile analysis reveals a gradient in the average Co valence state from the core to the surface of the A8 particle after 100 cycles, while A0 displays a relatively uniform profile (Figure 6c). Postcycling morphological analysis (Figure 6d) reveals a higher porosity in A8 (0.82%) compared to A0 (0.35%), indicative of increased microcrack formation. Structural characterization shows a pronounced shift of the 003 peak to lower angles in the XRD pattern of cycled A8, suggesting more severe lattice damage (Figure S33). Collectively, these results demonstrate that the dopant-free A0 material retains robust structural integrity and highly reversible reactions during prolonged cycling. By contrast, Al doping introduces chemical and structural heterogeneity at the pristine state, which exacerbates reaction inhomogeneity within particles during cycling. This inhomogeneity is further amplified by 2D defects, which impede lithium diffusion and destabilize oxygen atoms. Consequently, defect regions within microsized particles emerge as critical weak spots for structural degradation, characterized by oxygen release and crack initiation. This failure mechanism is corroborated by cross-sectional SEM images of cycled A8 electrodes (Figure 6e), which reveal cracks with a distinct twin-like morphology. Microcracks are symmetrically distributed along the primary boundary cracks (indicated by the dashed yellow line), exhibiting a mirror-like pattern. These observations strongly indicate that accelerated degradation is concentrated at defect regions, particularly at twin boundaries, within the Al-doped LCO structure. The robust structural stability of dopant-free LCO was further validated by assembling full cells with a silicon-graphite composite (Si/Gr) anode (Figures S34 and S35). In accordance with the half-cell testing conditions, the cutoff voltages were set at 4.44 V for A0 and 4.52 V for A8. When adjusted to achieve comparable initial capacities, A0 and A8 delivered 190.26 mAh/g and 192.63 mAh/g at 0.1 C, respectively. Notably, A0 retains 91.0% of its capacity (189.19 mAh/g) after 200 cycles at 0.5 C, significantly outperforming A8, which retains only 45.1% of its capacity (181.79 mAh/g at 0.5 C) (Figure 6f). The highly reversible cycling behavior of A0 is further evidenced by its stable voltage profile and consistent Coulombic efficiency over extended cycling (Figure S36). Additionally, full-cell testing also highlights the significantly enhanced rate performance of undoped LCO (A0) (Figure 6g), which is essential for practical applications in portable electronic devices.

3. DISCUSSION

Reflecting on the development of LCO materials, various elements have been doped into the LCO lattice to improve its electrochemical performance. As summarized from the literature data (Figure S37; Tables S4 and S5), doping enables LCO cathodes to operate at elevated cutoff voltages such as 4.6 V, 4.65 V, and higher, However, the capacity gains remain modest, particularly during extended cycling. Most charge−discharge tests reported in the literature were conducted at relatively high C-rates (0.5 C or above), with charge−discharge capacities generally remaining below 210 mAh/g. These conditions did not significantly induce the H1−3 phase transition in LCO. Notably, the undoped LCO investigated in this work ranks among the best-performing large-sized LCO materials, offering both high capacity and stable cycling (Note S2). These observations underscore two pivotal aspects that merit our attention. First, capacity, rather than voltage, is more directly tied to the high-voltage phase transitions in layered oxides, as interlayer gliding stems from repulsive interactions between hybridized TM-O orbitals mediated by vacant lithium sites.[10] When developing high-voltage oxide cathode materials, greater emphasis should be placed on the actual capacity achieved at elevated voltages.[25,33] Second, whether doping can genuinely suppress or inhibit the H1−3 phase transition in LCO remains a question, given the limited capacity improvements observed during cycling. Our results indicate that while Al doping effectively delays the onset voltage of the H1−3 phase transition, it does not alter the onset capacity. Similar phenomena have been observed in NCM cathodes, where Al doping has minimal impact on O1 phase formation and even reduces the capacity threshold for high-voltage transitions.[43,44] Once the high-voltage phase transition is activated (i.e., cycling with capacities >215 mAh/g in LCO), rapid performance degradation ensues. These findings highlight the necessity of addressing fundamental challenges associated with high-voltage phase transitions in all layered oxides, not limited to LCO. This issue has been under investigation for decades, yet it appears far from resolved. Strategies to delay the onset capacity of such transitions to higher values warrant further exploration. Alternative approaches, including Li-site doping or introducing chemical disorder, should be reassessed with a focus on capacity enhancement.[5,45]

As for doping, it remains a widely adopted modification strategy in both academia and industry, with well-documented benefits for oxide cathode materials. These include collective stabilization of bulk and surface properties, such as mitigated lattice variations and side reactions, improved thermal stability, and optimized secondary particle structures.[20,21] Although the main findings of this work may appear to contradict these conventional understandings at first glance, we would like to emphasize two key considerations for future studies on doping in cathode materials. First, a fair and meaningful comparison is essential to accurately evaluate the role of doping. For instance, the significantly reduced capacity of A8 at 4.6 V necessitates adjusting the cutoff voltage to achieve a comparable capacity or energy density relative to the undoped sample. Second, the effects of doping on the surface and bulk phases are inherently intertwined. Therefore, when discussing the specific mechanism of a dopant, caution should be taken to avoid drawing conclusions solely based on the overall electrochemical performance. In our study, surface-related influences were effectively decoupled through surface treatment, enabling us to isolate and examine the intrinsic effects of Al doping on the bulk phase.

Indeed, doping has played a pivotal role in advancing LCO from 4.2 V in the earliest commercial applications to the current 4.5 V, where stable lattice frameworks can be maintained at moderate levels of delithiation (Note S3). However, in the high-capacity regime, the inherent fragility of highly delithiated structures demands a comprehensive evaluation of doping-induced effects. Practical synthesis processes frequently result in deviations from the idealized substitution of single atomic sites during doping, leading to challenges such as nonuniform dopant distribution, defect formation, strain accumulation, and impurity phases that can compromise the anticipated benefits of doping. This phenomenon is expected to become increasingly significant as traditional high-voltage material designs require higher doping concentrations and a broader range of dopants (e.g., compositionally complex or high-entropy doping) to ensure structural stability.[23,24] Thus, it is critical to confront the negative consequences of the realistic doping strategy and meticulously balance its benefits against its drawbacks. In fact, our study proposes a completely different strategy wherein the bulk phase remains entirely undoped, resulting in a material with reduced defect density. This approach eliminates the risk of introducing defects through doping, thereby ensuring the structure stability upon high-voltage cycling. Here, we highlight the importance of a more nuanced doping strategy in the design of high-energy-density cathode materials, seeking to optimize their benefits while minimizing potential drawbacks through precise control.

4. CONCLUSIONS

In this study, we systematically explore the impact of Al doping on the chemistry, structure, high-voltage phase transition behavior, and electrochemical performance of LCO materials. While Al doping delays the onset voltage of the high-voltage H1−3 phase transition, it does not affect the onset capacity triggering slab gliding. Moreover, Al doping introduces increased chemical and structural heterogeneity, whereas the undoped LCO retains nearly perfect crystallization. This particle-level structural heterogeneity, manifesting as defective boundary regions, significantly hinders lithium diffusion and destabilizes oxygen atoms. In terms of energy density, Al-doped LCO shows marginal improvement, while undoped LCO achieves unprecedented cycling and rate performance. Enhancing the energy density of layered oxide cathode materials remains a persistent goal, with the high-voltage phase transition in the bulk structure posing a significant challenge. While substantial progress has been achieved in improving high-voltage performance through element doping, our findings highlight the need for future research to prioritize delaying the onset capacity of phase transitions, with a particular focus on maximizing energy density gains. Fundamental questions, such as the regulation and evolution of irreversible phase transitions, remain unresolved and demand further investigation. Additionally, while doping is a widely implemented strategy, its potential drawbacks warrant careful and comprehensive evaluation. Addressing these issues is essential for advancing high-energy-density, long-standing layered oxide cathode materials.

■ ASSOCIATED CONTENT

Supporting Information

The Supporting Information is available free of charge at https://pubs.acs.org/doi/10.1021/jacs.5c05162.

> Additional details about the experimental and theoretical methods, supporting notes, and additional characterization data, including Figures S1−S37, Notes S1−S3, and Tables S1−S5 (PDF)

■ AUTHOR INFORMATION

Corresponding Authors

Xiqian Yu − *Beijing Frontier Research Center on Clean Energy, Institute of Physics, Chinese Academy of Sciences, Beijing 100190, China; Center of Materials Science and Optoelectronics Engineering, University of Chinese Academy* *of Sciences, Beijing 100049, China;* orcid.org/0000-0001-8513-518X; Email: xyu@iphy.ac.cn

Lin Gu − *Beijing National Center for Electron Microscopy and Laboratory of Advanced Materials, School of Materials Science and Engineering, Tsinghua University, Beijing 100084, China;* Email: lingu@tsinghua.edu.cn

Hong Li − *Beijing Frontier Research Center on Clean Energy, Institute of Physics, Chinese Academy of Sciences, Beijing 100190, China; Center of Materials Science and Optoelectronics Engineering, University of Chinese Academy of Sciences, Beijing 100049, China;* orcid.org/0000-0002-8659-086X; Email: hli@iphy.ac.cn

Authors

Sichen Jiao − *Beijing Frontier Research Center on Clean Energy, Institute of Physics, Chinese Academy of Sciences, Beijing 100190, China*

Yu Li − *Beijing Frontier Research Center on Clean Energy, Institute of Physics, Chinese Academy of Sciences, Beijing 100190, China*

Ting Lin − *Beijing National Center for Electron Microscopy and Laboratory of Advanced Materials, School of Materials Science and Engineering, Tsinghua University, Beijing 100084, China*

Shuhang Feng − *Beijing Frontier Research Center on Clean Energy, Institute of Physics, Chinese Academy of Sciences, Beijing 100190, China*

Chengzhen Zhang − *Beijing Frontier Research Center on Clean Energy, Institute of Physics, Chinese Academy of Sciences, Beijing 100190, China*

Hongyi Pan − *Beijing Frontier Research Center on Clean Energy, Institute of Physics, Chinese Academy of Sciences, Beijing 100190, China*

Weiguang Lin − *Beijing Frontier Research Center on Clean Energy, Institute of Physics, Chinese Academy of Sciences, Beijing 100190, China*

Xuejie Huang − *Beijing Frontier Research Center on Clean Energy, Institute of Physics, Chinese Academy of Sciences, Beijing 100190, China;* orcid.org/0000-0001-5900-678X

Liquan Chen − *Beijing Frontier Research Center on Clean Energy, Institute of Physics, Chinese Academy of Sciences, Beijing 100190, China*

Complete contact information is available at:
https://pubs.acs.org/10.1021/jacs.5c05162

Author Contributions

[#]S.J., Y.L., and T.L. contributed equally to this work.

Notes

The authors declare no competing financial interest.

■ ACKNOWLEDGMENTS

The work was supported by funding from the National Natural Science Foundation of China (Grant Nos. 52325207, 22239003, 22393904, 52025025, and 52250402) and the National Key Research and Development Program (2022YFB2502200, 2021YFB2500300, and 2022YFB2404400). Dr. T.L. thanks the financial assistance from the Shuimu Tsinghua Scholar Program. The X-ray total scattering experiments were performed at the beamline BL08W of SPring-8. The nanoscale X-ray transmission microscopy experiment was performed at beamline BL18B, and the synchrotron X-ray diffraction experiment was performed at beamline BL14B at the Shanghai Synchrotron Radiation Facility (SSRF, China). The authors gratefully acknowledge the technical help from Dr. Yapei Li for NMR measurements and Dr. Biao Deng and Dr. Ling Zhang for their support in TXM-XANES experiments.

■ REFERENCES

(1) Goodenough, J. B.; Kim, Y. Challenges for rechargeable Li batteries. *Chem. Mater.* **2010**, *22*, 587−603.

(2) Manthiram, A. A reflection on lithium-ion battery cathode chemistry. *Nat. Commun.* **2020**, *11* (1), 1550.

(3) Mizushima, K.; Jones, P. C.; Wiseman, P. J.; Goodenough, J. B. L. ($0 < x < 1$): A new cathode material for batteries of high energy density. *Mater. Res. Bull* **1980**, *15*, 783−789.

(4) Wang, K.; Wan, J.; Xiang, Y.; Zhu, J.; Leng, Q.; Wang, M.; Xu, L.; Yang, Y. Recent advances and historical developments of high voltage lithium cobalt oxide materials for rechargeable Li-ion batteries. *J. Power Sources* **2020**, *460*, 228062.

(5) Wang, Q.; Yao, Z.; Wang, J.; Guo, H.; Li, C.; Zhou, D.; Bai, X.; Li, H.; Li, B.; Wagemaker, M.; Zhao, C. Chemical short-range disorder in lithium oxide cathodes. *Nature* **2024**, *629*, 341−347.

(6) Huang, W.; Li, J.; Zhao, Q.; Li, S.; Ge, M.; Fang, J.; Chen, Z.; Yu, L.; Huang, X.; Zhao, W.; et al. Mechanochemically robust $LiCoO_2$ with ultrahigh capacity and prolonged cyclability. *Adv. Mater.* **2024**, *36*, 2405519.

(7) Liu, T.; Yu, L.; Liu, J.; Dai, A.; Zhou, T.; Wang, J.; Huang, W.; Li, L.; Li, M.; Li, T.; Huang, X.; Xiao, X.; Ge, M.; Ma, L.; Zhuo, Z.; Amine, R.; Chu, Y. S.; Lee, W. K.; Wen, J.; Amine, K. Ultrastable cathodes enabled by compositional and structural dual-gradient design. *Nat. Energy* **2024**, *9*, 1252−1263.

(8) Zhang, M.; Kitchaev, D. A.; Lebens-Higgins, Z.; Vinckeviciute, J.; Zuba, M.; Reeves, P. J.; Grey, C. P.; Whittingham, M. S.; Piper, L. F.; Van der Ven, A.; Meng, Y. S. Pushing the limit of 3d transition metal-based layered oxides that use both cation and anion redox for energy storage. *Nat. Rev. Mater.* **2022**, *7*, 522−540.

(9) Chen, Z.; Lu, Z.; Dahn, J. R. Staging phase transitions in Li_xCoO_2. *J. Electrochem. Soc.* **2002**, *149*, A1604.

(10) Croguennec, L.; Pouillerie, C.; Mansour, A. N.; Delmas, C. Structural characterisation of the highly deintercalated LixNi1.02O2 phases (with $x \leq 0.30$). *J. Mater. Chem.* **2001**, *11*, 131−141.

(11) Liu, T.; Liu, J.; Li, L.; Yu, L.; Diao, J.; Zhou, T.; Li, S.; Dai, A.; Zhao, W.; Xu, S.; Ren, Y.; Wang, L.; Wu, T.; Qi, R.; Xiao, Y.; Zheng, J.; Cha, W.; Harder, R.; Robinson, I.; Wen, J.; Lu, J.; Pan, F.; Amine, K. Origin of structural degradation in Li-rich layered oxide cathode. *Nature* **2022**, *606*, 305−312.

(12) Bi, Y.; Tao, J.; Wu, Y.; Li, L.; Xu, Y.; Hu, E.; Wu, B.; Hu, J.; Wang, C.; Zhang, J. G.; Qi, Y.; Xiao, J. Reversible planar gliding and microcracking in a single-crystalline Ni-rich cathode. *Science* **2020**, *370*, 1313−1317.

(13) Tan, S.; Shadike, Z.; Li, J.; Wang, X.; Yang, Y.; Lin, R.; Cresce, A.; Hu, J.; Hunt, A.; Waluyo, I.; Ma, L.; Monaco, F.; Cloetens, P.; Xiao, J.; Liu, Y.; Yang, X. Q.; Xu, K.; Hu, E. Additive engineering for robust interphases to stabilize high-Ni layered structures at ultra-high voltage of 4.8 V. *Nat. Energy* **2022**, *7*, 484−494.

(14) Zhou, T.; Wang, J.; Lv, L.; Li, R.; Chen, L.; Zhang, S.; Zhang, H.; Ma, B.; Huang, J.; Wu, B.; Chen, L.; Deng, T.; Fan, X. Anion−π interaction and solvent dehydrogenation control enable high-voltage lithium-ion batteries. *Energy Environ. Sci.* **2024**, *17*, 9185−9194.

(15) Cai, M.; Dong, Y.; Xie, M.; Dong, W.; Dong, C.; Dai, P.; Zhang, H.; Wang, X.; Sun, X.; Zhang, S.; Yoon, M.; Xu, H.; Ge, Y.; Li, J.; Huang, F. Stalling oxygen evolution in high-voltage cathodes by lanthurization. *Nat. Energy* **2023**, *8*, 159−168.

(16) Zhang, J. N.; Li, Q.; Ouyang, C.; Yu, X.; Ge, M.; Huang, X.; Hu, E.; Ma, C.; Li, S.; Xiao, R.; Yang, W.; Chu, Y.; Liu, Y.; Yu, H.; Yang, X. Q.; Huang, X.; Chen, L.; Li, H. Trace doping of multiple elements enables stable battery cycling of $LiCoO_2$ at 4.6 V. *Nat. Energy* **2019**, *4*, 594−603.

(17) Yan, Y.; Fang, Q.; Kuai, X.; Zhou, S.; Chen, J.; Zhang, H.; Wu, X.; Zeng, C.; Wu, Z.; Zhang, B.; et al. One-step surface-to-bulk modification of high-voltage and long-life $LiCoO_2$ cathode with concentration gradient architecture. *Adv. Mater.* **2024**, *36*, No. e2308656.

(18) Liu, Q.; Su, X.; Lei, D.; Qin, Y.; Wen, J.; Guo, F.; Wu, Y. A.; Rong, Y.; Kou, R.; Xiao, X.; Aguesse, F.; Bareno, J.; Ren, Y.; Lu, W.; Li, Y. Approaching the capacity limit of lithium cobalt oxide in lithium ion batteries via lanthanum and aluminium doping. *Nat. Energy* **2018**, *3*, 936−943.

(19) Lee, S. B.; Park, N. Y.; Prak, G. T.; Kim, U. H.; Sohn, S. J.; Kang, M. S.; Ribas, R. M.; Monteiro, R. S.; Sun, Y. K. Doping strategy in developing Ni-rich cathodes for high-performance lithium-ion batteries. *ACS Energy Lett.* **2024**, *9*, 740−747.

(20) Yao, Y.; Xue, Z.; Li, C.; Li, J.; He, J.; Zhang, X.; Xiang, Y. Progress and perspective of doping strategies for lithium cobalt oxide materials in lithium-ion batteries. *Energy Storage Mater.* **2024**, *71*, 103666.

(21) Cui, Z.; Li, X.; Bai, X.; Ren, X.; Ou, X. A comprehensive review of foreign-ion doping and recent achievements for nickel-rich cathode materials. *Energy Storage Mater.* **2023**, *57*, 14−43.

(22) Faenza, N. V.; Pereira, N.; Halat, D. M.; Vinckeviciute, J.; Bruce, L.; Radin, M. D.; Mukherjee, P.; Badway, F.; Halajko, A.; Cosandey, F.; Grey, C. P.; Van der Ven, A.; Amatucci, G. G. Phase evolution and degradation modes of R-3m $Li_xNi_{1-y-z}Co_yAl_zO_2$ electrodes cycled near complete delithiation. *Chem. Mater.* **2018**, *30*, 7545−7574.

(23) Zhang, R.; Wang, C.; Zou, P.; Lin, R.; Ma, L.; Yin, L.; Li, T.; Xu, W.; Jia, H.; Li, Q.; Sainio, S.; Kisslinger, K.; Trask, S. E.; Ehrlich, S. N.; Yang, Y.; Kiss, A. M.; Ge, M.; Polzin, B. J.; Lee, S. J.; Xu, W.; Ren, Y.; Xin, H. L. Compositionally complex doping for zero-strain zero-cobalt layered cathodes. *Nature* **2022**, *610*, 67−73.

(24) Zhang, R.; Wang, C.; Zou, P.; Lin, R.; Ma, L.; Li, T.; Hwang, I.; Xu, W.; Sun, C.; Trask, S.; Xin, H. L. Long-life lithium-ion batteries realized by low-Ni, Co-free cathode chemistry. *Nat. Energy* **2023**, *8*, 695−702.

(25) Cui, Z.; Guo, Z.; Manthiram, A. Assessing the intrinsic roles of key dopant elements in high-nickel layered oxide cathodes in lithium-based batteries. *Adv. Energy Mater.* **2023**, *13*, 2203853.

(26) Yang, Z.; Mu, L.; Hou, D.; Rahman, M. M.; Xu, Z.; Liu, J.; Nordlund, D.; Sun, C.; Xiao, X.; Lin, F. Probing dopant redistribution, phase propagation, and local chemical changes in the synthesis of layered oxide battery cathodes. *Adv. Energy Mater.* **2020**, *11*, 2002719.

(27) Duffiet, M.; Blangero, M.; Cabelguen, P. E.; Song, K. S.; Fauth, F.; Delmas, C.; Carlier, D. Probing Al Distribution in LiCo0.96Al0.04O2 Materials Using 7Li, 27Al, and 59Co MAS NMR Combined with Synchrotron X-ray Diffraction. *Inorg. Chem.* **2020**, *59*, 2890−2899.

(28) Liu, X.; Xu, G. L.; Kolluru, V. S. C.; Zhao, C.; Li, Q.; Zhou, X.; Liu, Y.; Yin, L.; Zhuo, Z.; Daali, A.; Fan, J. J.; Liu, W.; Ren, Y.; Xu, W.; Deng, J.; Hwang, I.; Ren, D.; Feng, X.; Sun, C.; Huang, L.; Zhou, T.; Du, M.; Chen, Z.; Sun, S. G.; Chan, M. K. Y.; Yang, W.; Ouyang, M.; Amine, K. Origin and Regulation of Oxygen Redox Instability in High-Voltage Battery Cathodes. *Nat. Energy* **2022**, *7*, 808−817.

(29) Li, S.; Yao, Z.; Zheng, J.; Fu, M.; Cen, J.; Hwang, S.; Jin, H.; Orlov, A.; Gu, L.; Wang, S.; Chen, Z.; Su, D. Direct Observation of Defect-Aided Structural Evolution in a Nickel-Rich Layered Cathode. *Angew. Chem., Int. Ed.* **2020**, *59*, 22092−22099.

(30) Xu, Z.; Hou, D.; Kautz, D. J.; Liu, W.; Xu, R.; Xiao, X.; Lin, F. Charging Reactions Promoted by Geometrically Necessary Dislocations in Battery Materials Revealed by In Situ Single-Particle Synchrotron Measurements. *Adv. Mater.* **2020**, *32*, 2003417.

(31) Jiang, Y.; Yan, P.; Yu, M.; Li, J.; Jiao, H.; Zhou, B.; Sui, M. Atomistic Mechanism of Cracking Degradation at Twin Boundary of $LiCoO_2$. *Nano Energy* **2020**, *78*, 105364.

(32) Nguyen, H.; Silverstein, R.; Zaveri, A.; Cui, W.; Kurzhals, P.; Sicolo, S.; Bianchini, M.; Seidel, K.; Clement, R. J. Twin Boundaries Contribute to the First Cycle Irreversibility of $LiNiO_2$. *Adv Funct Mater* **2024**, *34*, 2306168.

(33) Gent, W. E.; Busse, G. M.; House, K. Z. The Predicted Persistence of Cobalt in Lithium-Ion Batteries. *Nat. Energy* **2022**, *7*, 1132−1143.

(34) Wang, Y.; Zhang, Q.; Xue, Z. C.; Yang, L.; Wang, J.; Meng, F.; Li, Q.; Pan, H.; Zhang, J. N.; Jiang, Z.; Yang, W.; Yu, X.; Gu, L.; Li, H. An In Situ Formed Surface Coating Layer Enabling $LiCoO_2$ with Stable 4.6 V High-Voltage Cycle Performances. *Adv. Energy Mater.* **2020**, *10*, 2001413.

(35) Levasseur, S.; Menetrier, M.; Suard, E.; Delmas, C. Evidence for Structural Defects in Non-Stoichiometric HT-$LiCoO_2$: Electrochemical. In *Electronic Properties, and ^{7}Li NMR Studies*; Solid State Ionics, 2000, Vol. *128*, pp. 11−24.

(36) Aydinol, M. K.; Kohan, A. F.; Ceder, G.; Cho, K.; Joannopoulos, J. J. Ab Initio Study of Lithium Intercalation in Metal Oxides and Metal Dichalcogenides. *Phys. Rev. B* **1997**, *56*, 1354−1365.

(37) Wang, Y.; Cheng, T.; Yu, Z. E.; Lyu, Y.; Guo, B. Study on the Effect of Ni and Mn Doping on the Structural Evolution of $LiCoO_2$ under 4.6 V High-Voltage Cycling. *J. Alloys Compd.* **2020**, *842*, 155827.

(38) Park, G. T.; Ryu, J. H.; Kim, J. H.; Sun, H. H.; Suh, D. E.; Han, S. M.; Park, N. Y.; Sun, Y. K. Aluminum-Distribution-Dependent Microstructural Evolution of NCA Cathodes: Is Aluminum Homogeneity Really Favorable? *Energy Storage Mater.* **2024**, *70*, 103496.

(39) Hu, T.; Dai, F. Z.; Zhou, G.; Wang, X.; Xu, S. Unraveling the Dynamic Correlations between Transition Metal Migration and the Oxygen Dimer Formation in the Highly Delithiated Li_xCoO_2 Cathode. *J. Phys. Chem. Lett.* **2023**, *14*, 3677−3684.

(40) Fu, F.; Wang, X.; Zhang, L.; Yang, Y.; Chen, J.; Xu, B.; Ouyang, C.; Xu, S.; Dai, F. Z.; E, W. Unraveling the Atomic-Scale Mechanism of Phase Transformations and Structural Evolutions during (De)-lithiation in Si Anodes. *Adv Funct Mater.* **2023**, 33, 2303936.

(41) Zhou, L.; Fu, X. P.; Wang, R.; Wang, C. X.; Luo, F.; Yan, H.; Jia, C. J.; Li, J.; Liu, J. C. Dynamic Phase Transitions Dictate the Size Effect and Activity of Supported Gold Catalysts. *Sci. Adv.* **2024**, *10*, No. eadr4145.

(42) Bian, R.; He, R.; Pan, E.; Li, Z.; Cao, G.; Meng, P.; Chen, J.; Liu, Q.; Zhong, Z.; Li, W.; Liu, F. Developing Fatigue-Resistant Ferroelectrics Using Interlayer Sliding Switching. *Science* **2024**, *385*, 57−62.

(43) Yu, D.; Zeng, G.; Chen, D.; Yan, Y.; Zou, Y.; Liu, Q.; Zhang, K.; Fang, K.; Xu, J.; Yin, W.; Hong, Y. H.; Qiu, T.; Liao, H. G.; Kuai, X.; Sun, Y.; Qiao, Y.; Sun, S. G. Revealing Gliding-Induced Structural Distortion in High-Nickel Layered Oxide Cathodes for Lithium-Ion Batteries. *ACS Nano* **2024**, *18*, 27654−27664.

(44) Adamo, J. B.; Manthiram, A. Understanding the Effects of Al and Mn Doping on the H2−H3 Phase Transition in High-Nickel Layered Oxide Cathodes. *Chem. Mater.* **2024**, *36*, 6226−6236.

(45) Huang, Y.; Zhu, Y.; Fu, H.; Ou, M.; Hu, C.; Yu, S.; Hu, Z.; Chen, C. T.; Jiang, G.; Gu, H.; Lin, H.; Luo, W.; Huang, Y. Mg-Pillared $LiCoO_2$: Toward Stable Cycling at 4.6 V. *Angew. Chem., Int. Ed.* **2021**, *60*, 4682−4688.